IOP Publishing and International Atomic Energy Agency Nuclear Fusion
Nucl. Fusion **52** (2012) 063026 (14pp) doi:10.1088/0029-5515/52/6/063026

Pfirsch–Schlüter current-driven edge electric fields and their effect on the L–H transition power threshold

A.Y. Aydemir

Institute for Fusion Studies, The University of Texas at Austin, Austin, TX 78712, USA

E-mail: aydemir@mail.utexas.edu

Received 8 November 2011, accepted for publication 9 May 2012
Published 1 June 2012
Online at stacks.iop.org/NF/52/063026

Abstract
An important contribution to the magnetohydrodynamic equilibrium at the tokamak edge comes from the Pfirsch–Schlüter current. The parallel electric field that can be associated with these currents is necessarily poloidally asymmetric and makes a similarly nonuniform contribution to the radial electric field on a flux surface. Here the role of the poloidal variation of this radial electric field in the L–H transition power threshold is investigated. Dependence of the resulting electric fields on magnetic topology, geometric factors such as the upper/lower triangularity and elongation, and the relative position of the X-point(s) in the poloidal plane are examined in detail. Starting with the assumption that an initially more negative radial electric field at the edge helps lower the transition power threshold, we find that our results are in agreement with a variety of experimental observations. In particular, for a 'normal' configuration of the plasma current and toroidal field we show the following. (i) The net radial electric field contribution by the Pfirsch–Schlüter currents at the plasma edge is negative for a lower single null and positive for a corresponding upper single null geometry. (ii) It becomes more negative as the X-point height is reduced. (iii) It also becomes more negative as the X-point radius is increased. These observations are consistent with the observed changes in the L–H transition power threshold $P_{\rm LH}$ under similar changes in the experimental conditions. In addition we find that (iv) in USN with an unfavourable ion ∇B drift direction, the net radial electric field contribution is positive but decreases as the X-point radius decreases. This is consistent with the C-Mod observation that an L–I mode transition can be triggered by increasing the upper triangularity in this configuration. (v) Locally the radial electric field is positive above the outer mid-plane and reverses sign with reversal of the toroidal field, consistent with DIII-D observations in low-power L-mode discharges. Thus, taken as a whole, the Pfirsch–Schlüter current-driven fields can explain a number of observations on the L–H or L–I transition and the required power threshold $P_{\rm LH}$ levels not captured by simple scaling laws. They may indeed be an important 'hidden variable'.

(Some figures may appear in colour only in the online journal)

1. Introduction

Success of the next generation device ITER [1] is predicated upon its operating in the high-confinement regime (H-mode) [2], characterized by improved particle and energy confinement. Transition to this enhanced confinement regime, where the energy confinement time can be a factor of 2 or more higher, is generally attributed to turbulence suppression and the formation of a transport barrier at the edge due to shearing of turbulent eddies by the $\boldsymbol{E} \times \boldsymbol{B}$ flows generated by a negative radial electric field well [3–7].

Although the L–H transition is sometimes observed in purely ohmic discharges, where it can be triggered by a sawtooth heat-pulse [8], it generally requires auxiliary heating power in excess of a machine-dependent threshold, $P_{\rm LH}$. In the absence of a quantitative understanding of the transition itself, a theoretical prediction for the power threshold in existing machines, let alone in ITER, has been difficult. Currently, based on data from major tokamaks around the world, there exists only an empirical scaling law of the form [9]

$$P_{\rm LH} = 0.042 \bar{n}_{\rm e}^{0.73} B_{\rm tor}^{0.74} S^{0.98}\ [\rm MW], \qquad (1)$$

where $\bar{n}_{\rm e}$ is the line-averaged density ($10^{20}\,\rm m^{-3}$), $B_{\rm tor}$ is the toroidal field [T], and S is a measure of the plasma surface area ($\rm m^2$).

However, as with all scaling laws, equation (1) is imperfect in its predictions, and there are wide variations in the actual power levels observed. For instance, in NSTX, a low aspect ratio device, the threshold can be a factor of 5–6 higher

than expected from this simple scaling law [10], and in general there tend to be significant differences even among machines running with similar global parameters. More importantly there are variations in $P_{\rm LH}$ obviously not captured by equation (1), leading to theories of possible 'hidden variables' [11]. Of these variations, the best-known example is the almost universal factor of 2 or more increase in $P_{\rm LH}$ when the ion $\boldsymbol{\nabla} B$-drift ($V_{\nabla Bi}$) points away from the active X-point [12]. There are also indications that the relative location of the X-point in the poloidal plane, $(R_{\rm X}, Z_{\rm X})$, plays an important role, with $P_{\rm LH}$ decreasing with decreasing X-point height, $Z_{\rm X}$ [13–16], or increasing radius, $R_{\rm X}$ [10, 15]. A more ambiguous issue, again related to the $V_{\nabla Bi}$ direction, is the sensitive dependence of $P_{\rm LH}$ on the exact magnetic topology: ASDEX Upgrade (AUG), and the small aspect ratio tokamaks NSTX and MAST find that $P_{\rm LH}$ is a minimum for a balanced double-null (DN) configuration [17], whereas C-Mod and DIII-D see the lowest power threshold for a lower/upper single null (LSN/USN) configuration with the $V_{\nabla Bi}$ in the direction of the X-point [18, 19]. Results from DIII-D are qualified by the observation that the DN configuration may actually have a similar or lower threshold than a single-null depending on triangularity [15, 20], thus once again pointing to the important role the plasma shape may be playing in setting $P_{\rm LH}$.

Of course there are many other effects, such as the neutral pressure outside the separatrix, and (lithium) wall conditioning that also strongly influence the $P_{\rm LH}$ levels (see, for instance, [10, 21, 22]). However, these are beyond the scope of this work, where we focus mainly on geometric and topological effects.

1.1. Poloidal electric field

The charge separation due to guiding centre drifts, or equivalently, the non-solenoidal diamagnetic current, is prevented by a parallel 'return current' [23], which can be calculated by demanding that the total current be divergence-free, $\nabla \cdot \boldsymbol{J} = \nabla \cdot (\boldsymbol{J}_\perp + J_\parallel \boldsymbol{B}/B) = 0$. In our (ψ, θ, ζ) flux coordinate system where we write the magnetic field as $\boldsymbol{B} = \boldsymbol{\nabla}\psi \times \boldsymbol{\nabla}\zeta + F(\psi)\boldsymbol{\nabla}\zeta$, this requirement leads to

$$J_\parallel B = F p' \left(1 - \frac{B^2}{\langle B^2\rangle}\right) + \frac{B^2}{\langle B^2\rangle}\langle J_\parallel B\rangle. \tag{2}$$

The first term on the right is the Pfirsch–Schlüter current, and the second can be associated with an externally driven contribution such as the ohmic current. The angular-brackets denote the usual flux-surface average: $\langle A\rangle \equiv \oint A\mathcal{J}\,\mathrm{d}\theta / \oint \mathcal{J}\,\mathrm{d}\theta$, where the Jacobian $\mathcal{J} = 1/\boldsymbol{\nabla}\psi\cdot\boldsymbol{\nabla}\theta\times\boldsymbol{\nabla}\zeta$.

The parallel electric field associated with this current, the radial electric field that can be obtained from it, and the effect of this radial field and its poloidal variation on the L–H transition are the main topics of this work. To calculate this field, we start with Ohm's law of the form [24]

$$\boldsymbol{E} = -\boldsymbol{\nabla}\phi + \frac{V_l}{2\pi}\boldsymbol{\nabla}\zeta = -\boldsymbol{v}\times\boldsymbol{B} + \eta\boldsymbol{J} - \frac{\boldsymbol{B}}{B^2}\nabla\cdot\eta_{\rm H}\boldsymbol{\nabla}\frac{J_\parallel B}{B^2}, \tag{3}$$

which, in addition to the resistive term, includes a hyper-resistivity ($\eta_{\rm H}$) contribution that will be used to model the effects of edge turbulence. With $B^\psi = \boldsymbol{B}\cdot\boldsymbol{\nabla}\psi = 0$, $B^\theta = \boldsymbol{B}\cdot\boldsymbol{\nabla}\theta = -1/\mathcal{J}$, $B^\zeta = \boldsymbol{B}\cdot\boldsymbol{\nabla}\zeta = F/R^2$, we have

$$E_\parallel B = -\frac{E_\theta}{\mathcal{J}} + \frac{V_l F}{2\pi R^2} = \eta J_\parallel B - \nabla\cdot\eta_{\rm H}\boldsymbol{\nabla}\frac{J_\parallel B}{B^2}, \tag{4}$$

where $E_\theta = -\partial\phi/\partial\theta$, and the Jacobian is given by $\mathcal{J} = -qR^2/F$ ($q(\psi) < 0$ with our sign convention for $\boldsymbol{B}$). Note that we have assumed $\boldsymbol{B}\cdot\boldsymbol{\nabla}p = 0$ and ignored the pressure gradient term in the Ohm's law. Since the potential ϕ is single-valued, $\oint(\partial\phi/\partial\theta)\,\mathrm{d}\theta = 0$ determines the loop voltage as

$$V_l = \langle E_\parallel B\rangle \oint \frac{\mathrm{d}\theta}{q\boldsymbol{B}\cdot\boldsymbol{\nabla}\theta} = \left(\eta\langle J_\parallel B\rangle - \left\langle\nabla\cdot\eta_{\rm H}\boldsymbol{\nabla}\frac{J_\parallel B}{B^2}\right\rangle\right) \times \oint \frac{\mathrm{d}\theta}{\boldsymbol{B}\cdot\boldsymbol{\nabla}\zeta}. \tag{5}$$

Finally, using equations (4) and (5) the poloidal electric field can be put in the form

$$E_\theta = -\frac{\partial\phi}{\partial\theta} = \frac{q}{F}\left(\frac{E_\parallel B}{1/R^2} - \frac{\langle E_\parallel B\rangle}{\langle 1/R^2\rangle}\right), \tag{6}$$

where we also made use of

$$\oint \frac{\mathrm{d}\theta}{\boldsymbol{B}\cdot\boldsymbol{\nabla}\theta} = \frac{2\pi q}{F\langle 1/R^2\rangle}. \tag{7}$$

Since the Pfirsch–Schlüter current is a robust feature of toroidal confinement valid in all collisionality regimes, here we have focused on its role in generating a poloidal and radial electric field at the tokamak edge. But clearly there are other physical mechanisms that contribute (see, for example, [3, 25]). In the Pfirsch–Schlüter regime, another important contribution comes from the parallel variation of density and temperature [26, 27]. This contribution has the same sign and poloidal variation as that generated by the Pfirsch–Schlüter current considered here; thus, its inclusion in our edge electric field calculations will not make a qualitative change in our results. Its quantitative effects will be examined elsewhere.

1.2. The potential and the radial electric field

Now the potential on a flux surface can be determined by integrating E_θ:

$$\phi(\psi,\theta) = \phi(\psi,0) - \int_0^\theta E_\theta(\psi,\theta')\,\mathrm{d}\theta', \tag{8}$$

where $\phi(\psi, 0)$ is an as yet undetermined integration constant.

Since there does not appear to be a way to determine this constant within the formalism of this work, we need to make use of additional pieces of physics. First, we invoke a result from our earlier initial value calculations with the 3D magnetohydrodynamic (MHD) code *CTD*; namely, the outer mid-plane is a stagnation point for poloidal flows. This follows directly from symmetry considerations for up–down symmetric DN configurations (the physics behind this is clear in figure 1 of [28]). The outer mid-plane remains a stagnation point even for USN/LSN configurations (figure 2 of [29]). This observation alone can be used to determine $\phi(\psi, 0)$ on each flux surface. But because of the ambiguity in defining where exactly the 'mid-plane' is where we set $u^\theta(\psi, \theta_{\rm mid}) = 0$, we choose another approach, namely minimization of the

energy in the electric field, which can be shown *a posteriori* to guarantee consistency with the results of the initial value calculations mentioned above.

Since the loop voltage is independent of the integration constant $\phi(\psi, 0)$, we will minimize only the energy in the field

$$\tilde{\boldsymbol{E}} \equiv \left(E_{\psi 0} - \frac{\partial \phi(\psi, 0)}{\partial \psi} \right) \nabla \psi + E_\theta \nabla \theta, \tag{9}$$

where $E_{\psi 0}$ is the value of the field with $\phi(\psi, 0) \to 0$:

$$E_{\psi 0} \equiv \int_0^\theta \frac{\partial E_\theta(\psi, \theta')}{\partial \psi} \, \mathrm{d}\theta'. \tag{10}$$

Then minimizing the energy

$$W_E = \frac{1}{2} \epsilon_0 \int \tilde{E}^2 \mathcal{J} \, \mathrm{d}\psi \mathrm{d}\theta \, \mathrm{d}\zeta \tag{11}$$

with respect to $\phi(\psi, 0)$ requires on each flux surface

$$\oint \left[\left(E_{\psi 0} - \frac{\partial \phi(\psi, 0)}{\partial \psi} \right) |\nabla \psi|^2 + E_\theta \nabla \psi \cdot \nabla \theta \right] \mathcal{J} \mathrm{d}\theta = 0, \tag{12}$$

which leads to

$$\frac{\partial \phi(\psi, 0)}{\partial \psi} = \frac{\langle \boldsymbol{E}_0 \cdot \nabla \psi \rangle}{\langle |\nabla \psi|^2 \rangle}, \tag{13}$$

where $\boldsymbol{E}_0 \equiv E_{\psi 0} \nabla \psi + E_\theta \nabla \theta$. Now the total field can be written as

$$\boldsymbol{E} = \left(E_{\psi 0} - \frac{\langle \boldsymbol{E}_0 \cdot \nabla \psi \rangle}{\langle |\nabla \psi|^2 \rangle} \right) \nabla \psi + E_\theta \nabla \theta + \frac{V_l}{2\pi} \nabla \zeta. \tag{14}$$

We can easily show that $\langle \boldsymbol{E} \cdot \nabla \psi \rangle = 0$. As a consequence, there is no net charge build up in any volume enclosed by a flux surface; charges are merely redistributed on the surface, which can be seen by integrating Poisson's equation:

$$\begin{aligned} \int_{\psi' > \psi} \nabla^2 \phi \mathcal{J} \, \mathrm{d}\psi' \, \mathrm{d}\theta \, \mathrm{d}\zeta &= - \oint \nabla \phi \cdot \nabla \psi \mathcal{J} \, \mathrm{d}\theta \, \mathrm{d}\zeta \\ &= 2\pi \langle \boldsymbol{E} \cdot \nabla \psi \rangle \oint \mathcal{J} \, \mathrm{d}\theta = 0. \end{aligned} \tag{15}$$

In this respect, the physics driving the electric fields in this work is different from the ion orbit loss mechanism of Shaing and Crume [3], and the X-point loss mechanism of Chang *et al* [25], both of which involve ion losses through the separatrix. Of course, this new mechanism is meant to complement, not replace them, as will be discussed more fully in the following section.

The simple variational principle used here to determine the flux function $\phi(\psi, 0)$ is not unique. We are also exploring others that may be more appropriate, but they are not expected to make qualitative changes in our results.

In the following sections we evaluate the electric field of equation (14) for various equilibrium configurations. We demonstrate correlations between some E-field-dependent metrics that will be defined below and the experimental changes in the transition power threshold, P_{LH}, as the plasma shape, magnetic topology, and other relevant parameters are modified.

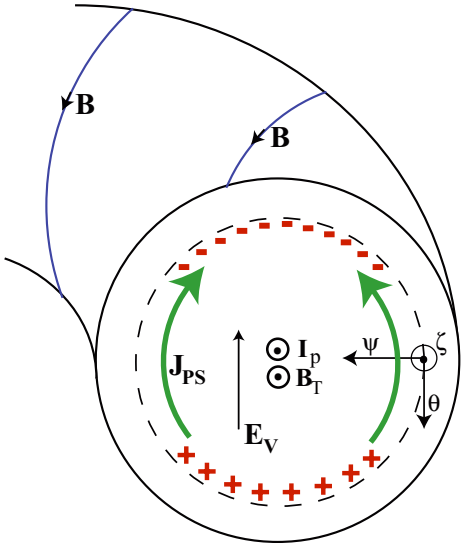

Figure 1. Charge separation that would develop in a purely toroidal field, and the poloidal projection of the parallel Pfirsch–Schlüter currents (green arrows) that neutralize it when there is a rotational transform. At the inboard (high-field) side, the currents are anti-parallel to the field (negative) and subtract from the ohmic current; they are positive on the low-field side. Also shown is the (ψ, θ, ζ) flux coordinate system used in this work. Note that $\nabla\psi \sim -\nabla r$, $\nabla\theta \sim -\nabla\theta_{\mathrm{p}}$, where $(r, \theta_{\mathrm{p}}, \zeta)$ is the usual orthogonal toroidal coordinate system.

2. Comparisons with experimental observations

The main thesis of this work is that the electric field of equation (14), driven by the collisional and turbulent modifications of the Pfirsch–Schlüter currents, plays an important role in determining the L–H transition power threshold, P_{LH}. However, our present view is that this field only modifies a background field $\boldsymbol{E}_{\mathrm{back}}$ produced by a different set of mechanisms, such as the ion orbit or the X-point loss physics referred to earlier. Since there is as yet no satisfactory theory of the L–H transition, here we only assume the existence of an $\boldsymbol{E}_{\mathrm{back}}$ with unspecified origins that is modified by the Pfirsch–Schlüter field of equation (14) such that

$$\boldsymbol{E}_{\mathrm{total}} = \boldsymbol{E}_{\mathrm{back}} + \boldsymbol{E}_{\mathrm{PS}}. \tag{16}$$

Generally $\boldsymbol{E}_{\mathrm{back}}$ is assumed to be a flux function, i.e. independent of the poloidal angle. Thus, $\boldsymbol{E}_{\mathrm{PS}}$, which exhibits a nearly sinusoidal variation on a flux surface (see figure 1; this point is demonstrated explicitly in figures 3 and 4), either adds to or subtracts from the background field, making the transition easier or more difficult in terms of the heating power requirement, depending on its net contribution to the total field.

In this section, using a free-boundary equilibrium code especially developed for this purpose, we demonstrate in a large number of configurations that the net variation in this field $\boldsymbol{E}_{\mathrm{PS}}$ qualitatively parallels the expected behaviour of P_{LH}, thus providing a strong support for our thesis. Lack of a quantitative understanding of the transition itself prevents us from being more quantitative in our predictions, since it is not clear how to translate a unit of change in the electric field metric used here to a change in the required auxiliary input power.

Below we briefly describe the equilibrium code before we discuss the computational results.

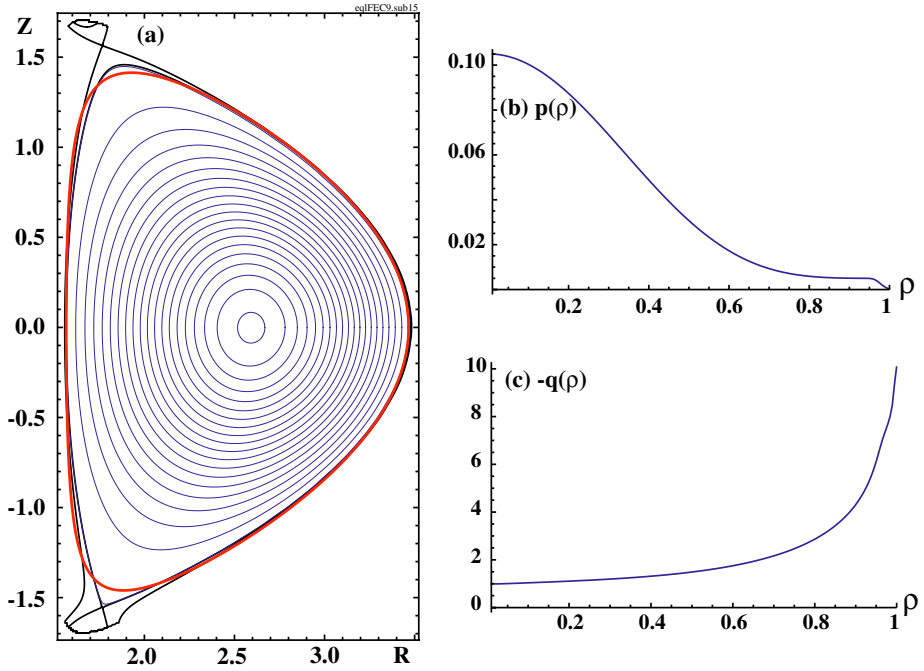

Figure 2. A sample equilibrium with a DN magnetic geometry. Here the lower X-point is the active one. The smooth red curve represents a four-parameter least-squares fit to the separatrix; it is used to define the effective values of the geometric parameters δ_U, δ_L, κ_U, and κ_L. On the right, the pressure and safety factor profiles are plotted as functions of normalized flux, $\rho \equiv (\psi_0 - \psi)/(\psi_0 - \psi_{sep})$.

2.1. The equilibrium code

The Grad–Shafranov equation in the non-dimensional form

$$-\Delta^*\psi \equiv -R^2\nabla\cdot\left(\frac{1}{R^2}\boldsymbol{\nabla}\psi\right) = R^2 p'(\psi) + F(\psi)F'(\psi) \tag{17}$$

is solved directly on an (R, Z) grid. Lengths are normalized to minor radius a so that $R \equiv R/a$. The magnetic field is normalized such that the toroidal field $B_{tor} \sim \mathcal{O}(R)$, and the poloidal field (PF) $B_p \sim \mathcal{O}(1)$. In particular, the poloidal current function $F \equiv RB_{tor} = R_0^2$ for a vacuum field, where R_0 is the normalized major radius.

The equilibrium is calculated in two steps. First, a fixed boundary equilibrium is obtained with a prescribed boundary curve parametrized as follows [30]:

$$\begin{aligned} R(\alpha) &= R_0 + \cos(\alpha + \Delta\sin\alpha), \\ Z(\alpha) &= Z_0 + \kappa\sin\alpha, \end{aligned} \tag{18}$$

where

$$\begin{aligned} \Delta &= \tfrac{1}{2}\left((\delta_U + \delta_L) + (\delta_U - \delta_L)\sin\alpha\right), \\ \kappa &= \tfrac{1}{2}\left((\kappa_U + \kappa_L) + (\kappa_U - \kappa_L)\sin\alpha\right), \end{aligned}$$

and α is an angle-like parameter in the (R, Z) plane. Here $(\kappa_U,\ \delta_U)$, and $(\kappa_L,\ \delta_L)$ are the elongation and triangularity for the upper and lower half, respectively. This step determines $\psi_{fixed}(R, Z)$, with the boundary condition $\psi_{fixed} = 0$ on the boundary curve of equation (18).

In the next step, a fixed external field, ψ_{ext}, generated by PF currents outside the boundary is calculated using the well-known Green's function for the Δ^*-operator (see, for example, [31]). This field is used to introduce one or more X-points in the magnetic configuration. Then equation (17) is solved again for ψ_{fixed} using the total flux $\psi = \psi_{fixed} + \psi_{ext}$ in the evaluation of the input functions on the right-hand side. In this step, the (inner) separatrix is defined as the plasma boundary. An example is shown in figure 2.

In the final, free-boundary equilibrium, the plasma boundary $\psi = \psi_{sep}$ is typically far removed from the initial fixed boundary curve. Using the parametrization defined by equation (18), a four-parameter least-squares-fit to the new boundary curve is obtained to find the new effective elongation and triangularity values for the upper and lower halves of the plasma cross-section. Such a fit is shown in figure 2(*a*) by the smooth red curve. Note that the fitting error is largest near the X-points, and elongations are typically underestimated by this procedure.

2.2. General properties of the $\boldsymbol{E}$*-field and* $\boldsymbol{E}\times\boldsymbol{B}$ *velocity*

For the purpose of evaluating the electric field at the edge, we use global parameters for a DIII-D-like discharge, with $B_{tor} = 2.1\,\mathrm{T}$, $I_p = 1\,\mathrm{MA}$, $\overline{n}_e = 2.5\times10^{19}\,\mathrm{m}^{-3}$, $n_{e\text{-sep}} = 10^{19}\,\mathrm{m}^{-3}$, $T_{e\text{-sep}} = 50\,\mathrm{eV}$, $R_0 = 1.66\,\mathrm{m}$, $a = 0.67\,\mathrm{m}$ [32]. With these we have the following: the characteristic Alfvén velocity, $v_A \equiv (a/R_0)B_{tor}/\sqrt{\mu_0 m_i n_i} = 3.7\times10^6\,\mathrm{m\,s}^{-1}$, the Alfvén time, $\tau_A \equiv a/v_A = 1.8\times10^{-7}\,\mathrm{s}$, the classical resistivity at the separatrix, $\eta_{sep} = 4.37\times10^{-6}\,\Omega\,\mathrm{m}$, and the resistive diffusion time, $\tau_R \equiv \mu_0 a^2/\eta = 1.3\times10^{-1}\,\mathrm{s}$, which gives a normalized resistivity of $\tilde{\eta} \equiv \tau_A/\tau_R = 1.4\times10^{-6}$.

An ad hoc hyper-resistivity (electron viscosity) coefficient η_H is used to incorporate edge-turbulence effects into the model. Its value is chosen such that this term in Ohm's law becomes important only for length scales shorter than a radial grid width, i.e.

$$\delta^2 = \frac{\eta_H}{\eta B^2} < (\delta r)^2. \tag{19}$$

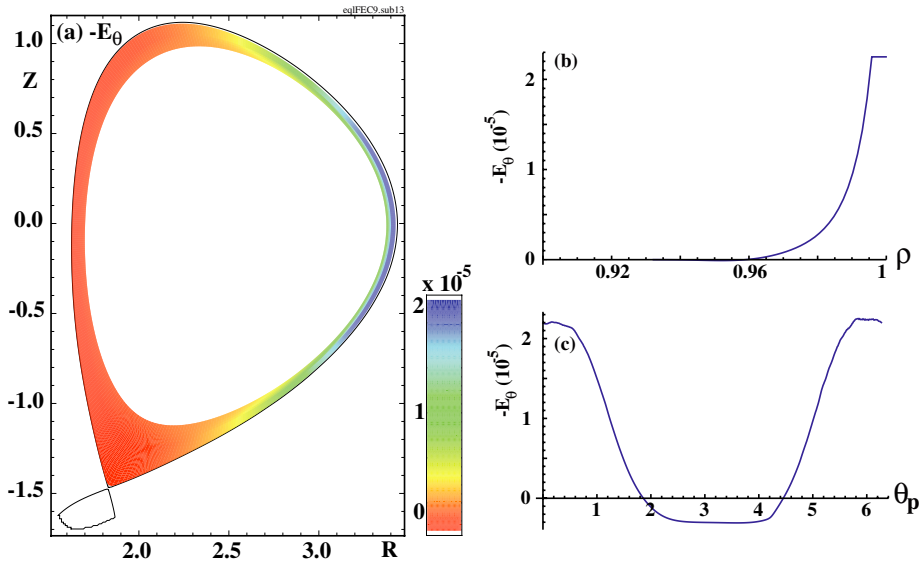

Figure 3. The poloidal electric field at the edge for a LSN configuration. (*a*) The field in a narrow region at the edge. The radial width of the computational domain shown has been magnified in order to make some of the details more easily visible. Note that the values are cut off beyond $\rho \simeq 0.995$. (*b*) The radial variation of $(-E_\theta)$ near the outer mid-plane where the field has its maximum. (*c*) The poloidal variation of the field on the 'last closed flux surface' (LCFS). The magnitude is given in dimensionless units. In the figures we have adopted the following conventions: (i) Unless otherwise specified, the ion ∇B drift direction is downwards. (ii) In order to avoid confusion, we use a more conventional coordinate system $(\rho, \theta_\mathrm{p})$ for the plots, where $\rho \equiv (\psi_0 - \psi)/(\psi_0 - \psi_\mathrm{sep})$, $\nabla\rho \sim -\nabla\psi$, and θ_p is not the flux coordinate θ but the usual poloidal angle that increases in the counter-clockwise direction, i.e. $\nabla\theta_\mathrm{p} \sim -\nabla\theta$.

For collisional plasmas $\eta_\mathrm{H}/\eta \leqslant 10^{-4}$ [33]; we use $\eta_\mathrm{H} = 10^{-4}\eta$ throughout this work.

Calculated under these (or very similar) conditions, a typical poloidal electric field profile, $E_\theta(\psi, \theta)$, is shown in figure 3. In this and other figures to follow, we actually plot the negatives of the field components, $(-E_\psi)$, $(-E_\theta)$, since the usual radial and poloidal vectors ∇r, $\nabla\theta_\mathrm{p}$ are in opposite directions to our flux coordinate vectors $\nabla\psi$, $\nabla\theta$, respectively: $E_r \simeq -E_\psi R B_\mathrm{p}$, and $E_p \simeq -E_\theta$.

We note that the field $(-E_\theta)$ is negative/positive on the inboard/outboard sides of the torus, respectively, in agreement with the physical picture presented in figure 1; roughly it is directed vertically upwards when the ion ∇B-drift direction is downwards. The poloidal variation can also be understood by extracting the dominant (Pfirsch–Schlüter) term in equation (6) and rewriting it in the form

$$E_{\theta,\mathrm{PS}} \simeq \frac{\eta(\psi) q(\psi) p'(\psi)}{\langle B^2 \rangle} R^2 \left(\langle B^2 \rangle - B^2 \right), \qquad (20)$$

and recalling that $q(\psi) < 0$, $p'(\psi) > 0$ in our flux coordinate system (ψ, θ, ζ). The reasons for the dominance of the field on the outboard side (mainly due to the R^2 term) and the in–out variation (due to the $(\langle B^2 \rangle - B^2)$ term) becomes obvious through equation (20). The large radial gradient is due to variations in the resistivity $\eta \sim p^{-3/2}$ and q profiles at the edge.

Dimensionless units are used in the figures. The electric field E can be converted to SI units using $E_\mathrm{SI} = (v_\mathrm{A} B_0) E$. Thus, with $v_\mathrm{A} = 3.7 \times 10^6\,\mathrm{m\,s^{-1}}$, $B_0 = 2.1(a/R_0)\,\mathrm{T}$, $a/R_0 = 0.67\,\mathrm{m}/1.66\,\mathrm{m}$ we have $v_\mathrm{A} B_0 = 3.14 \times 10^6\,\mathrm{V\,m^{-1}}$, and the maximum PF in figure 3 is $E_\theta \simeq 70\,\mathrm{V\,m^{-1}}$, near the outboard mid-plane.

Figure 4 shows $(-E_\psi)$, which is a measure of the radial electric field: $E_r \simeq -E_\psi R B_\mathrm{p}$, where $B_\mathrm{p} = |\nabla\psi|/R$ is the PF. Again, the field is dominant on the low-field side of the torus, and as expected from the physics driving it (see figure 1), approximately it is negative/positive in the lower/upper half-planes, respectively. Thus, in this configuration, the lower half-plane adds to the background field, which is assumed to be negative, and subtracts from it in the upper half-plane. Below we will use its flux-surface average $\langle -E_\psi \rangle$ to quantify its net contribution. Note that in dimensional units the radial electric field minimum in figure 4 is $E_r \simeq -3.7\,\mathrm{kV\,m^{-1}}$ in the lower half-plane about halfway between the X-point and the outer mid-plane.

Poloidal projection of the edge $\boldsymbol{E} \times \boldsymbol{B}$ flows generated by the electric field of equation (14) is shown in figure 5(*a*). The arrow heads indicate the direction of the flow and their colour the velocity amplitude. Using the same DIII-D global parameters as above, we have in dimensional units the maximum poloidal velocity $V_\mathrm{E} \simeq 3.7\,\mathrm{km\,s^{-1}}$. As expected, the poloidal flows have a stagnation point near the outer mid-plane; they are also in agreement with the edge flows generated in an earlier calculation with the 3D MHD code *CTD* that are shown in figure 5(*b*). An interesting feature of these $\boldsymbol{E} \times \boldsymbol{B}$ flows is that they provide an obvious neutral recycling path from the divertor region to the edge plasma within the separatrix.

2.3. Change in P_LH between LSN and USN magnetic geometries

A universal feature of the L–H transition is that the required heating power is a factor of 2 or more higher if the ion ∇B drift points away from the active X-point [12]. This change in P_LH is observed, for example, when the toroidal field direction

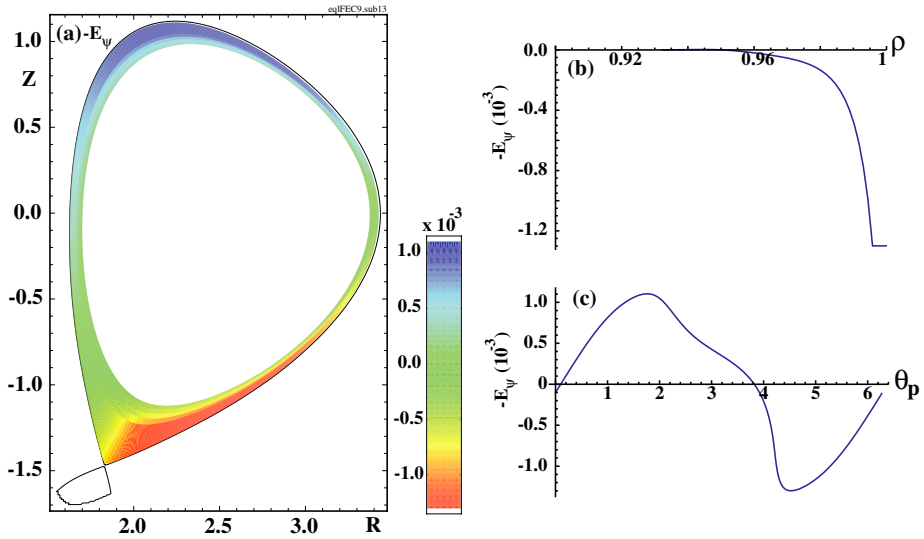

Figure 4. The radial electric field at the edge for a LSN configuration. (*a*) The field in a narrow region at the edge. The radial width of the computational domain has been magnified in order to make some of the details more easily visible. (*b*) The radial variation of $(-E_\psi)$ in the lower half-plane at a point where it has its minimum value. (*c*) The poloidal variation of the field on the 'last closed flux surface' (LCFS).

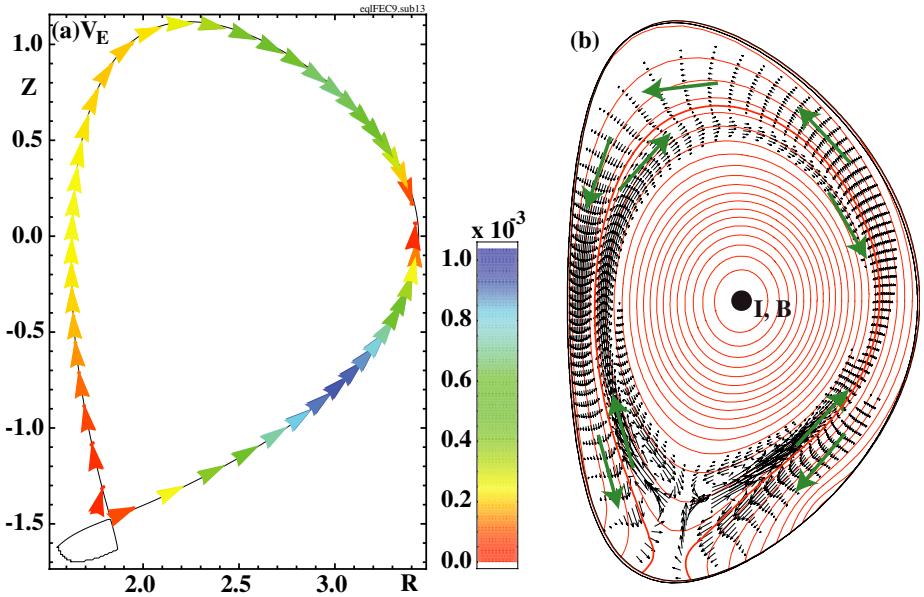

Figure 5. (*a*) The edge $\boldsymbol{E} \times \boldsymbol{B}$ flows (inside the separatrix) for a LSN configuration, as calculated by the equilibrium code. (*b*) Flows calculated with the 3D MHD code *CTD*, reproduced from figure 2 of [28] with permission (© 2009 IOP Publishing). Here both the inside and outside (scrape of layer (SOL)) flows are shown. Note that the flows within the separatrix in (*a*) and (*b*) are in qualitative agreement and both show a stagnation point near the outer mid-plane.

is reversed, thus reversing the ion ∇B drift direction with respect to a fixed magnetic (X-point) geometry [34]. Similarly, it can be observed by holding the toroidal field fixed while changing the magnetic geometry between lower (LSN) and USN configurations (e.g. [35]).

In this section we examine the changes in the Pfirsch–Schlüter current-induced electric field as the magnetic geometry is gradually varied between a LSN and USN while the ion ∇B drift is held fixed in the direction of the lower X-point. As figures of merit, we will use the flux-surface average of the radial electric field $\langle -E_\psi(\psi,\theta)\rangle = \langle \partial\phi/\partial\psi\rangle$ and that of the associated shearing rate $\langle \omega_S(\psi,\theta)\rangle$, where ω_S is defined as [4, 5]

$$\omega_S = \frac{(RB_p)^2}{B}\frac{\partial E_\psi}{\partial \psi}. \tag{21}$$

As mentioned earlier, the assumption here is that there is both a 'background' and a Pfirsch–Schlüter contribution $\langle -E_\psi\rangle$ to the total electric field such that a negative $\langle -E_\psi\rangle$ lowers P_{LH} and makes the L–H transition easier while a positive $\langle -E_\psi\rangle$ increases it. In fact, in this and the following sections we will see that a decreasing (increasing) $\langle -E_\psi\rangle$ is correlated with a lower (higher) P_{LH} under corresponding experimental conditions. Thus, although details of the function

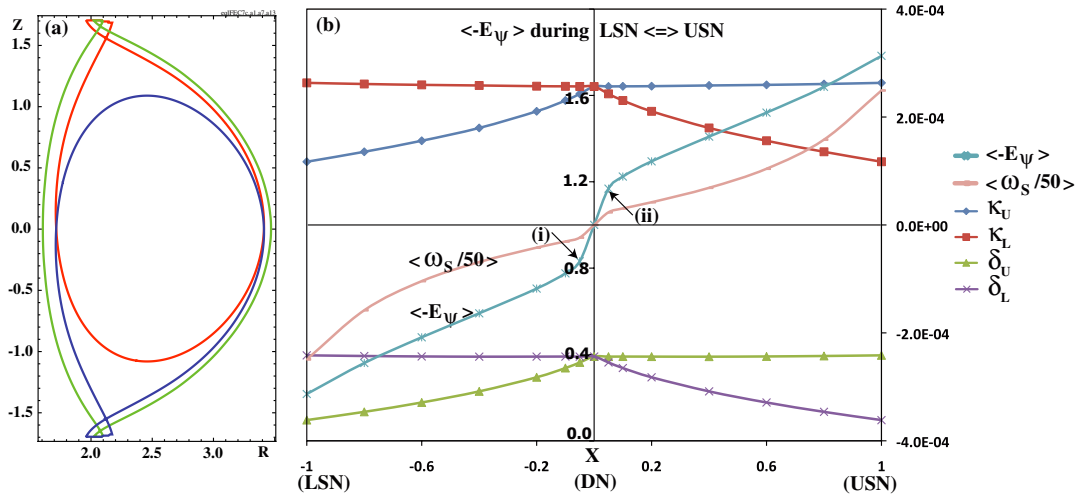

Figure 6. Changes in the electric field E_ψ and the shearing rate ω_s as the magnetic geometry is gradually varied from a LSN to USN. (a) The separatrices for LSN, USN, and a perfectly balanced DN configuration are shown. (b) Changes in the four parameters characterizing the plasma boundary shape, κ_U, κ_L, δ_U, δ_L (the centre axis) and the flux-surface averages $\langle -E_\psi \rangle$, $\langle \omega_S/50 \rangle$ (the right axis) are shown. Note that the shearing rate has been rescaled by a factor of 50. The horizontal axis is $X \equiv (I_{XU} - I_{XL})/(I_{XU} + I_{XL})$, where I_{XU}, I_{XL} are the currents in the upper and lower X-point PF coils, respectively. The separatrices for the two points labelled (i) and (ii) in (b) are plotted explicitly in figure 7.

f is not known at this point, we can say that the power threshold has the functional form

$$P_{LH} = f(\langle -E_\psi \rangle, \boldsymbol{\xi}), \qquad \text{with } \frac{\partial P_{LH}}{\partial \langle -E_\psi \rangle} > 0. \tag{22}$$

Here the vector $\boldsymbol{\xi}$ represents all other dependences, i.e. $\boldsymbol{\xi} = (B, \bar{n}_e, S, \ldots)$.

With equation (22) in mind, we now look at changes in various quantities during a LSN→USN scan, which are summarized in figure 6. In figure 6(a) the separatrices for a LSN, USN and the intermediate DN configuration demonstrate the change in the magnetic topology. In figure 6(b), variations in the four parameters κ_U, κ_L, δ_U, δ_L characterizing the plasma boundary shape, and the flux-surface averages of $(-E_\psi)$ and ω_S are shown. Unlike the other parameter scans discussed below, LSN→USN is a rather drastic modification of the boundary that involves changes in all four parameters, although the pair (κ_L, δ_L) is nearly constant during the LSN→DN phase, and (κ_U, δ_U) is constant during the DN→USN phase of the transition. Recall that these parameters are obtained by a least-squares fit to the separatrix and do not capture the variation near the X-points very accurately (see figure 2).

Of course the most important point about figure 6 is the change in $\langle -E_\psi \rangle$: in normalized units, it varies from -3.13×10^{-4} in full LSN to $+3.13 \times 10^{-4}$ in USN, a net change of about 2 kV m^{-1} in the flux-surface averaged radial electric field. In other words, the Pfirsch–Schlüter field adds to the background field in LSN and opposes it in USN. Note that $\langle \omega_S \rangle$ also exhibits a similar change between LSN and USN configurations. In LSN, the induced shear by $E_{\psi,PS}$ adds to that of the background field, thus enhancing it, whereas in USN, it reduces it.

An interesting feature of the $\langle -E_\psi \rangle$ variation in figure 6(b) is the nearly step-function jump it exhibits around the $X = 0$ (balanced DN) point. A similar jump is also seen in the $\langle \omega_S \rangle$ curve. This result may explain the highly sensitive dependence of P_{LH} on the 'imbalance of the two divertors' seen in DIII-D [15]. Apparently, for a discharge near but just below the threshold, the L–H transition can be triggered at a desired point in time by adjusting the balance between the upper and lower X-points in favour of the one in the ion ∇B direction.

As seen in figure 7(a), such an adjustment can involve not much more than a change in the location of the active X-point. Here the LSN (labelled (i)) and USN separatrices (ii) are essentially identical curves except near the X-points. The corresponding points in the LSN ↔ USN scan of figure 6(b) are indicated by arrows, where $X_i = -0.05$, $\langle -E_\psi \rangle_i = -6.73 \times 10^{-5}$, and $X_{ii} = +0.05$, $\langle -E_\psi \rangle_{ii} = +6.73 \times 10^{-5}$. The variable X measures the balance between the currents in the upper and lower X-point PF coils: $X \equiv (I_{XU} - I_{XL})/(I_{XU} + I_{XL})$.

The L–H transition when the plasma is pushed from state (ii) to (i) can be understood better by looking at it in the $(P_{aux}, \langle -E_\psi \rangle)$ plane of figure 7(b). Here the power threshold function $P_{LH}(\langle -E_\psi \rangle, \boldsymbol{\xi})$ is represented graphically by a line with a positive slope. At constant auxiliary heating power P_{aux}, point (ii) with $\langle -E_\psi \rangle_{ii} > 0$ is below the threshold but its antisymmetric part (i) with $\langle -E_\psi \rangle_i = -\langle -E_\psi \rangle_{ii} < 0$ is above it, thus triggering the L–H transition. Note that another important implication of this result is that the X-points play a crucial role in the transition physics, since the plasma boundary for the two configurations are almost identical except for the location of the X-point.

Briefly summarizing, with the ion ∇B drift pointing down, we have $\langle -E_{\psi,PS} \rangle < 0$ for a LSN, and $\langle -E_{\psi,PS} \rangle > 0$ for an USN; from symmetry, $\langle -E_{\psi,PS} \rangle = 0$ for a perfectly balanced DN. Based on these results, we would expect $P_{LH}^{LSN} < P_{LH}^{DN} < P_{LH}^{USN}$. This ordering of the L–H transition power threshold agrees with observations on, for example, DIII-D [19] and C-Mod [18], but it does not appear to be universally true [17]. In particular, in the spherical tokamaks MAST and

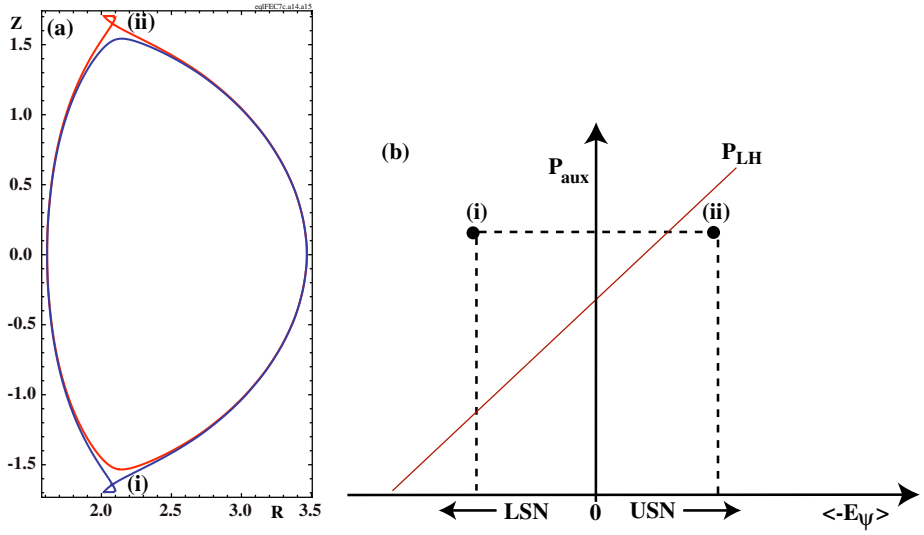

Figure 7. (*a*) Two configurations that differ mainly in the location of the active X-point with respect to the ion ∇B drift direction (pointing down). In the $LSN \leftrightarrow USN$ scan of figure 6(*b*), these correspond to the points labelled (i) and (ii) (indicated by arrows). (*b*) The power threshold function $P_{\rm LH}(\langle -E_\psi \rangle, \xi \simeq \text{const.})$ of equation (22) is represented by a line with a positive slope in the $(P_{\rm aux}, \langle -E_\psi \rangle)$ plane. Note that $\langle -E_\psi \rangle_{(i)} = -\langle -E_\psi \rangle_{(ii)}$. It is clear how the USN point (ii) can be below the threshold while the LSN point (i) below it, thus possibly explaining the sensitive dependence of $P_{\rm LH}$ on the 'imbalance of the two divertors' [15].

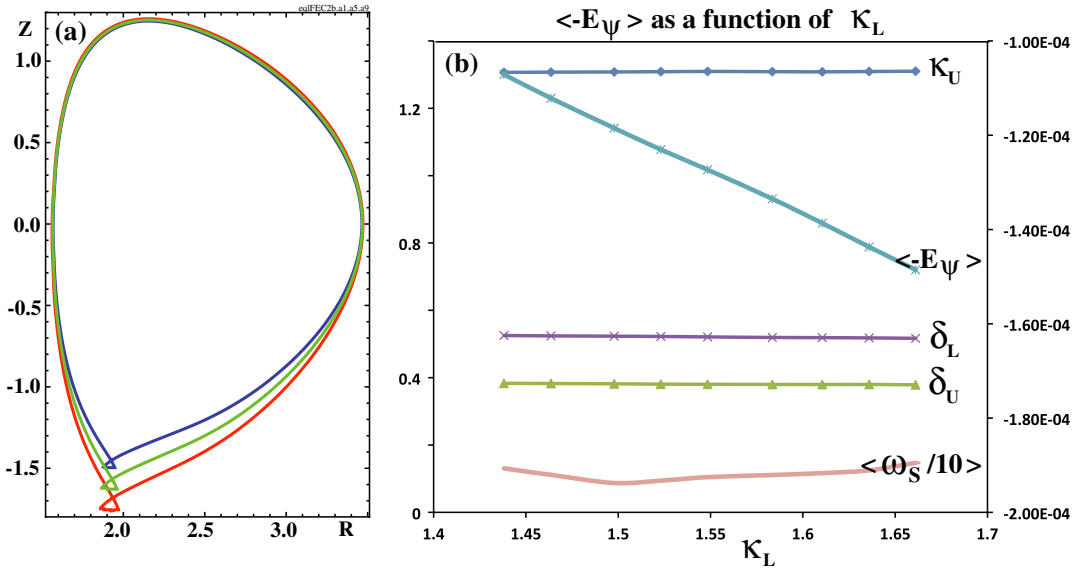

Figure 8. Changes in the net radial electric field $\langle -E_\psi \rangle$ as the X-point height ($Z_{\rm X}$) is reduced by varying the lower elongation $\kappa_{\rm L}$. (*a*) Separatrices for three different values of $\kappa_{\rm L}$. The X-point radius ($R_{\rm X}$) is essentially constant. (*b*) $\langle -E_\psi \rangle$ and the scaled shearing rate, $\langle \omega_{\rm S}/10 \rangle$ (the right scale). The remaining three parameters, $\kappa_{\rm U}$, $\delta_{\rm U}$, $\delta_{\rm L}$ are constant during the scan (the left scale). Note that the radial electric field becomes more negative as the X-point height decreases (as $\kappa_{\rm L}$ increases), leading to lower $P_{\rm LH}$.

NSTX, the DN configuration seems to have the lowest $P_{\rm LH}$, although at least in NSTX it is possible that this is only a local minimum, as the absolute lowest $P_{\rm LH}$ is apparently obtained in LSN [36]. But it is also possible that these experimental results need to be re-examined given the extreme sensitivity of $P_{\rm LH}$ to a shift in the location of the active X-point as seen both in DIII-D [15] and in our computational results discussed above (figures 6(*b*) and 7).

Below we will examine other changes in the plasma boundary and provide further confirmation for the positive correlation between $\langle -E_\psi \rangle$ and $P_{\rm LH}$ assumed in equation (22).

2.4. Role of the X-point height $Z_{\rm X}$

In a number of devices, the 'height' of the X-point is seen to affect the power threshold strongly, lower X-points resulting in significant reductions in $P_{\rm LH}$ [13–16]. Here we look at the changes in $\langle -E_{\psi,\rm PS} \rangle$ as the lower elongation $\kappa_{\rm L}$ is increased while keeping the other boundary parameters $\delta_{\rm L}$, $\kappa_{\rm U}$, $\delta_{\rm U}$ fixed, which effectively lowers the X-point while minimizing unwanted perturbations to the plasma boundary shape.

The results of this X-point height scan are summarized in figure 8. The lower elongation, $\kappa_{\rm L}$, varies between 1.44–1.66, while $\delta_{\rm L} \simeq 0.52$, $\kappa_{\rm U} \simeq 1.31$, $\delta_{\rm U} \simeq 0.38$. In

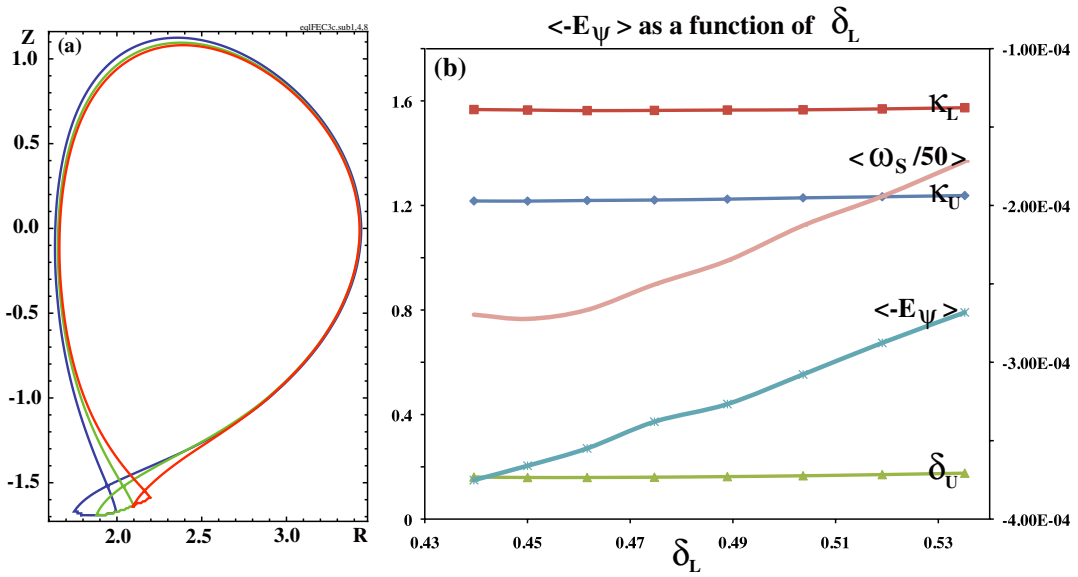

Figure 9. Changes in the net radial electric field $\langle -E_\psi \rangle$ as the X-point radius (R_X) is reduced by increasing the lower triangularity δ_L. (a) Separatrices for three different values of δ_L. The X-point height (Z_X) is essentially constant. (b) $\langle -E_\psi \rangle$ and the scaled shearing rate, $\langle \omega_S/50 \rangle$ (the right scale). The remaining three parameters, κ_U, κ_L, δ_U are constant during the scan (the left scale). Note that the radial electric field becomes more negative as the X-point radius increases (as δ_L decreases), leading to lower P_{LH}.

(a) the separatrices for three points from the scan, $\kappa_L = 1.44, 1.55, 1.66$, are shown, indicating that only the X-point height is varying, with very little change in its radius. Figure 8(b) shows that the net radial electric field, $\langle -E_\psi \rangle$, is negative, as expected from the LSN geometry with the ion drift pointing down, and as the lower elongation increases (the X-point height decreases), it becomes more negative. This change in $\langle -E_\psi \rangle$ with lower Z_X is also in agreement with JET measurements that show a more negative radial electric field at lower X-point height [14] and is consistent with the decrease in P_{LH} seen in, for example, NSTX [16], DIII-D [15], and JET [13, 14] with lower Z_X. Note that there is very little change in the net shearing rate, $\langle \omega_S \rangle$, during this scan, possibly implying that the depth of the radial electric field more than the shearing rate is the important parameter in setting P_{LH}.

2.5. Role of the X-point radius R_X

Stability of the pedestal is generally assumed to be governed by the edge-current driven peeling and pressure gradient driven ballooning modes [37, 38]. While triangularity has a stabilizing influence on these ideal MHD instabilities (see, for example, [39, 40]), ironically it also makes access to the H-mode more difficult by leading to higher P_{LH} values [10, 15].

Here we look at the changes in the Pfirsch–Schlüter current-induced radial electric field as the X-point is swept radially inwards by increasing lower triangularity, δ_L, while the remaining boundary-shape parameters are held fixed. The results are summarized in figure 9. In (a), the separatrices for $\delta_L = 0.44, 0.49, 0.54$ are shown at constant values of $\kappa_U \simeq 1.22$, $\kappa_L \simeq 1.56$, and $\delta_U \simeq 0.17$. In (b), the net radial electric field $\langle -E_\psi \rangle$ is negative but becomes less so as the lower triangularity is increased. Again, a less negative net contribution to the total edge radial electric field is correlated with the experimentally observed increase in P_{LH}. Note that here the net shearing rate $\langle \omega_S \rangle$ also exhibits a similar behaviour, becoming less negative with increasing δ_L. In NSTX, this correlation between increasing X-point radius and lower P_{LH} was explained in terms of increased X-point losses (thus higher E_r) seen in the XGC0 code at lower B [41]. The mechanism proposed here is in agreement in terms of its net effect on the edge radial electric field but does not depend on ion losses through the separatrix.

2.6. Role of triangularity in the I-mode transition

Up to this point we have been describing the possible role of the Pfirsch–Schlüter current-induced edge electric fields in setting the L–H transition power threshold. The same physics can be used to explain a particular feature of the transition to I-mode observed in C-Mod [42] that at first seems difficult to understand, as it contradicts some of the observations on the L–H transition discussed above.

The I-mode appears to be an intermediate stage between L-mode with its 'low' energy and particle confinement and H-mode where both the energy and particle confinement show a dramatic improvement. In I-mode, the energy confinement improves, leading to a temperature pedestal at the edge, but the particle confinement retains its L-mode character. As such, the I-mode represents an ideal confinement regime, avoiding density, ash, and impurity buildup without the deleterious effects of large edge-localized modes (ELMs), while at the same time leading to higher core temperatures.

I-mode is typically observed in discharges with an unfavourable ion drift direction (USN with the ∇B drift pointing down) at auxiliary heating power levels below the threshold for the L–H transition itself; thus, empirically $P_{LI} < P_{LH}$. A puzzling feature of the L–I transition is that it can be triggered by increasing the upper triangularity [42], i.e. by reducing the X-point radius R_X, which is the exact opposite of what one would expect from the observations on the L–H transition discussed in the previous section: the L–H transition

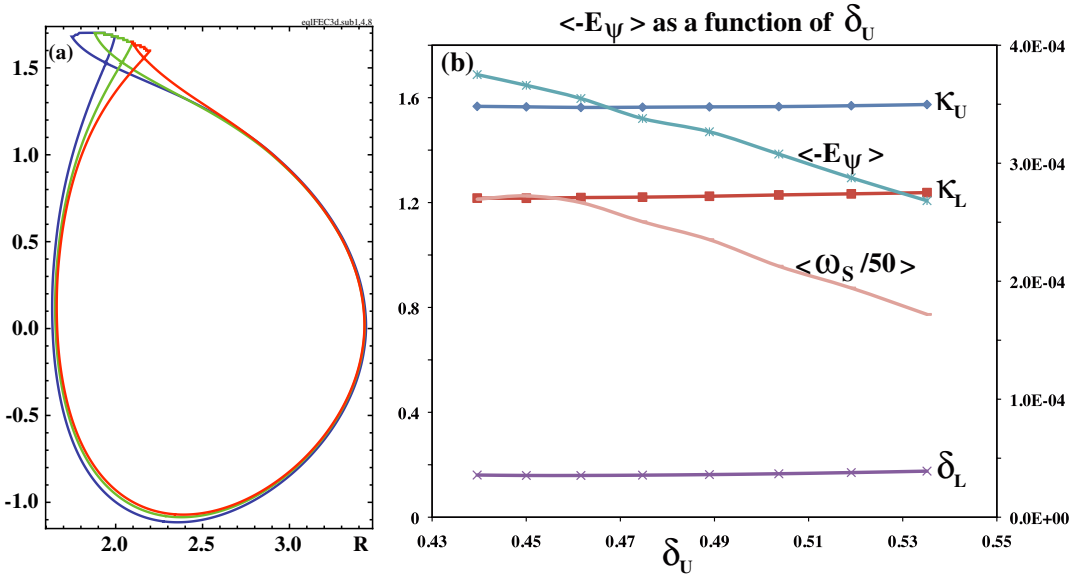

Figure 10. Changes in the net radial electric field $\langle -E_\psi \rangle$ as the X-point radius (R_X) is reduced by increasing the upper triangularity δ_U in an USN magnetic geometry. (a) Separatrices for three different values of δ_U. The X-point height (Z_X) is essentially constant. (b) $\langle -E_\psi \rangle$ and the scaled shearing rate, $\langle \omega_S/50 \rangle$ (the right scale). The remaining three parameters, κ_U, κ_L, δ_L are constant during the scan (the left scale). Note that the radial electric field is positive and decreases as the X-point radius decreases with increasing δ_U, triggering an L–I transition at some point. This behavior is the exact opposite of what is seen in the LSN configuration of figure 9.

in LSN has a lower threshold at larger R_X and can be triggered by decreasing lower triangularity. This point can be resolved by examining $\langle -E_\psi \rangle$ under conditions that trigger an L–I transition.

Although the same results can be deduced using symmetry arguments and figure 9, we have explicitly examined the variation of $\langle -E_\psi \rangle$ for an USN with the ion ∇B drift in the unfavourable direction (pointing down) as the upper triangularity (thus R_X) is varied. The results are shown in figure 10. Again, figure 10(a) shows the variation of the plasma boundary (the separatrix) as δ_U is varied between 0.44 and 0.54, while keeping the remaining boundary parameters approximately constant. In figure 10(b), we see that the net radial electric field is positive, as expected from this magnetic geometry and ion drift direction, and it becomes less positive as δ_U increases. A similar behaviour is observed for the net shearing rate $\langle \omega_S \rangle$.

Again, examined in the $(P_{aux}, \langle -E_\psi \rangle)$ plane, it becomes clear how an L–I transition can be triggered by a positive Pfirsch–Schlüter contribution that becomes less positive as the triangularity is increased (figure 11(a)). Here we assume a lower power threshold for the L–I transition, with a similar functional dependence on $\langle -E_\psi \rangle$:

$$P_{LI} = g(\langle -E_\psi \rangle, \xi) < P_{LH}(\langle -E_\psi \rangle, \xi), \quad \frac{\partial P_{LI}}{\partial \langle -E_\psi \rangle} > 0. \quad (23)$$

In the USN configuration of figure 11(a), $\langle -E_\psi \rangle > 0$ but decreases in the direction of increasing δ_U (recall figure10(b)). Thus, while point (1) is below the L–I threshold, at a fixed auxiliary heating power level, the discharge can be pushed above P_{LI} at a higher δ_U (point (2)). In fact, it should be possible to trigger an I–H transition by increasing the triangularity even further (point (3)). Physically, these transitions with the unfavourable drift direction are made possible by a decreasing opposition to the transition by the Pfirsch–Schlüter current-driven radial electric field as it becomes less positive.

Similar arguments will show that I-mode in LSN with the ion drift in the favourable direction should occur at higher triangularity than H-mode. Figure 11(b) shows the possible transitions for a LSN geometry. Recall that now $\langle -E_\psi \rangle < 0$ and increases (becomes less negative) with increasing lower triangularity (recall figure 9(b)). Then point (4) in L-mode can be pushed into I-mode at constant P_{aux} by decreasing δ_L (point (5)); an I–H mode transition is possible with a further decrease in δ_L (point (6)).

2.7. Edge radial electric field comparison with low-power DIII-D observations

Pfirsch–Schlüter currents provide a robust mechanism for generating edge electric fields that should be observable under a wide variety of experimental conditions. However, since there are clearly other contributions to E_r, e.g., from pressure gradients and neutral beam-driven flows, L-mode discharges with low auxiliary heating power may provide the cleanest experimental conditions for such a measurement.

In fact, there is such a measurement in a low-power L-mode discharge in DIII-D, and interestingly the edge electric field E_r is seen to change sign when the toroidal field is reversed in a LSN geometry [34]. This sign reversal cannot be understood in terms of ion orbit [3] or X-point loss mechanisms [25], since these will always lead to a negative E_r. But the transformation $E_r \to -E_r$ when $B_{tor} \to -B_{tor}$ follows trivially from the physics of the Pfirsch–Schlüter currents and the associated edge electric fields. When B_{tor} is reversed, ∇B drift direction and the direction of the return current, i.e., the Pfirsch–Schlüter current in figure 1, are both reversed, thus reversing both the PF E_θ and the potential ϕ of equation (6).

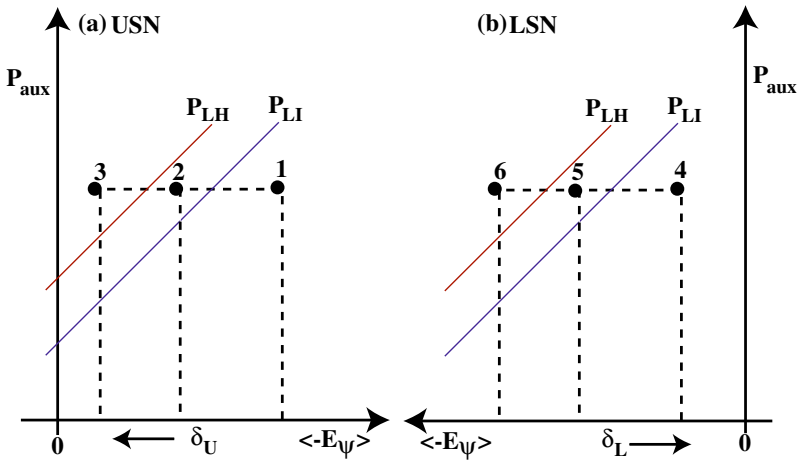

Figure 11. (a) Evolution of an USN discharge in the $(P_{\rm aux}, \langle -E_\psi \rangle)$ plane in response to changes in upper triangularity; $\delta_{\rm U}$ increases in the direction of the arrow. In addition to the $P_{\rm LH}(\langle -E_\psi \rangle, \xi = {\rm const})$ line (equation (22)), a $P_{\rm LI}(\langle -E_\psi \rangle, \xi = {\rm const})$ line with similar characteristics is shown. Point (1) in L-mode can transition to I-mode (point (2)) with increasing $\delta_{\rm L}$. From there it should be possible to enter H-mode (point (3)) with a further increase in triangularity. (b) For a LSN discharge, the trajectory is reversed. The sequence of transitions L–I–H requires decreasing $\delta_{\rm L}$. In general, I-mode should be more common at higher triangularity.

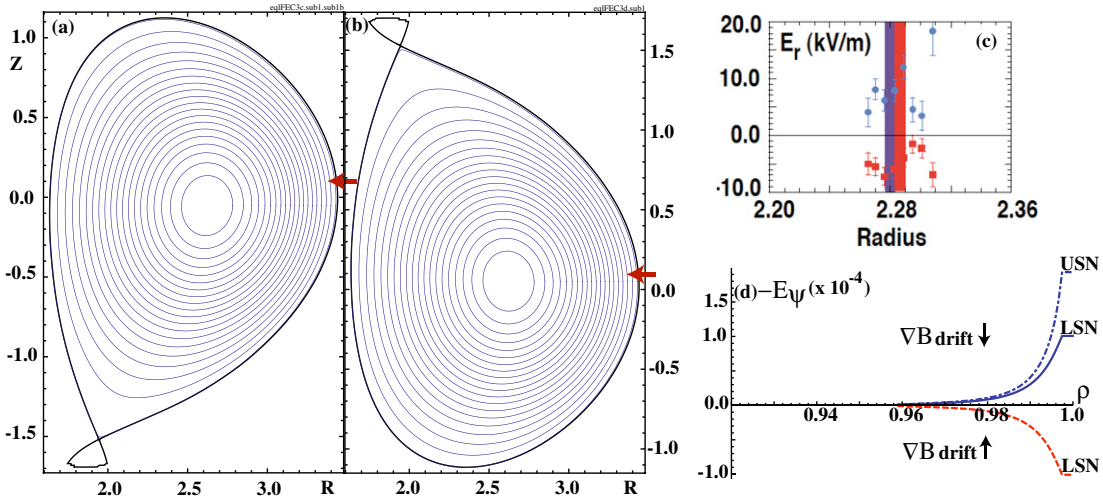

Figure 12. Edge radial electric field reverses sign when the toroidal field is reversed. In (a) and (b) flux surfaces for lower and USN geometries used in the calculations are shown. The arrows indicate the approximate location of the fixed point in the (R, Z) plane where the experimental and computational measurements of E_r are made. (c) Experimental results from a low-power, L-mode, LSN discharge in DIII-D, reproduced from [34] with permission (© 2000 European Physical Society) (figure 1(f)). The blue circles are for $B_{\rm tor} > 0$ (ion ∇B drift towards the X-point). The red squares are for $B_{\rm tor} < 0$. (d) Normalized $(-E_\psi) \simeq E_r/(RB_{\rm p})$ due to Pfirsch–Schlüter currents. The dotted–dashed blue line is for USN, and the solid blue line is for LSN, both with $B_{\rm tor} > 0$. The red dashed line is for LSN with $B_{\rm tor} < 0$.

Reversal of the radial electric field follows trivially since $E_\psi = -\partial\phi/\partial\psi$.

The experimental measurements from DIII-D are compared with our computational results in figure 12. Since $E_\psi = E_\psi(\psi, \theta)$, for this purpose a point near but slightly above the mid-plane is chosen, indicated by arrows in figures 12(a) and (b), which is approximately where the charge exchange recombination (CER) spectroscopy measurements in DIII-D appear to have been made. Figure 12(c) is reproduced from [34] and shows the edge E_r for ion ∇B drift pointing towards (blue circles) and away from (red squares) the X-point in a LSN. In (d) the numerical results are shown; $E_r \simeq -E_\psi R B_{\rm p} > 0$ with the favourable drift direction and negative otherwise, in agreement with the DIII-D results. In a subsequent series of experiments in DIII-D where the toroidal field direction was held fixed but the magnetic geometry was changed between an upper and LSN, E_r was found to be positive in both USN and LSN [35]. As seen in figure 12(d), this observation is also consistent with our calculations since E_r remains positive in the upper half-plane regardless of the location of the X-point; its sign is determined by the absolute direction of the ∇B drift, not its relative direction with respect to the X-point.

3. Summary and discussion

The parallel 'return current' of equation (2) develops in response to a non-solenoidal diamagnetic current in the toroidal geometry; equivalently, we can say that it represents a parallel flow of charges connecting the top and bottom of a toroidal surface to neutralize the charge separation that

would result from charge-dependent ∇B and curvature drifts (figure 1). At the collisional edge, near the separatrix, there can be a significant parallel electric field associated with this current. Its poloidal component, as shown in equation (6), and more explicitly in equation (20), vanishes at two critical points, $(R_c, Z_c)_U$, $(R_c, Z_c)_L$, one each in the upper and lower half-planes, respectively, where $B^2 \simeq \langle B^2 \rangle$ (figure 3(*c*); the equality is exact if the ohmic contribution is ignored):

$$E_\theta[(R_c, Z_c)_U] = E_\theta[(R_c, Z_c)_L] = 0. \tag{24}$$

Location of these points in the poloidal plane is determined to a large degree by the plasma boundary shape.

Since $\partial\phi/\partial\theta = -E_\theta$, these critical points are also where the potential has its extrema. Also, using making use of $\partial E_\psi/\partial\theta = \partial E_\theta/\partial\psi$, and assuming that the flux surface shape and equilibrium quantities do not vary very fast between neighbouring flux surfaces, we see that E_ψ also attains maximum and minimum values on a flux surface at approximately the same points (see plots of $-E_\theta(\theta_p)$ and $-E_\psi(\theta_p)$ in figures 3(*c*) and 4(*c*)). Thus, near the separatrix we have

$$\begin{aligned}(-E_\psi(\theta))_{max} &\simeq -E_\psi[(R_c, Z_c)_U],\\ (-E_\psi(\theta))_{min} &\simeq -E_\psi[(R_c, Z_c)_L].\end{aligned} \tag{25}$$

Recalling that $(-E_\psi) \simeq E_r/RB_p$, we see that equation (25) is consistent with the physical picture presented in figure 1. Note that here we have assumed a 'normal' configuration for the plasma current and toroidal field, as shown in figure 1. If the toroidal field (thus the ∇B drift direction) is reversed, the extrema for the radial electric field would change places: the maximum/minimum would be in the lower/upper half-plane.

The properties of the radial electric field, as measured by $(-E_\psi) \simeq E_r/RB_p$ of equation (14), have been the focus of much of this work. Since $(-E_\psi)$ is poloidal angle-dependent, we have chosen to use its flux-surface average, $\langle -E_\psi \rangle$, along with that of the shearing rate w_S (equation (21)), as figures of merit to determine whether a particular magnetic configuration should have a higher or lower L–H transition power threshold, P_{LH}, compared with others.

For a diverted tokamak, there is one or two additional critical points, the X-points, where $B_p^2 = 0$. We find that the location of the X-point(s), (R_X, Z_X), with respect to the critical points of equations (24), $(R_c, Z_c)_{U,L}$, where $E_\theta = 0$ and E_ψ has an approximate extremum, plays a crucial role in determining $\langle -E_\psi \rangle$ and $\langle w_S \rangle$, and thus the contribution to the power threshold P_{LH} by the Pfirsch–Schlüter current-driven electric fields. A clear example can be seen by revisiting the results of section 2.5, where we examined how changing the X-point radius R_X affects $\langle -E_\psi \rangle$ and thus P_{LH} in a LSN geometry (see figure 9). Changes in the net radial electric field and shearing rate of figure 9(*b*) can be understood by looking at how the fields at the edge respond to a change in lower triangularity δ_L, which in turn affects the X-point radius R_X. In figure 13 various quantities on a flux surface near the separatrix are shown as functions of the poloidal angle θ_p (recall that $\nabla\theta_p \sim -\nabla\theta$, where θ is the flux coordinate). The solid red lines are for $\delta_L = 0.44$, and the dashed blue lines for $\delta_L = 0.54$. As seen in figure 13(*a*), both the poloidal electric field amplitude around the flux surface and the critical

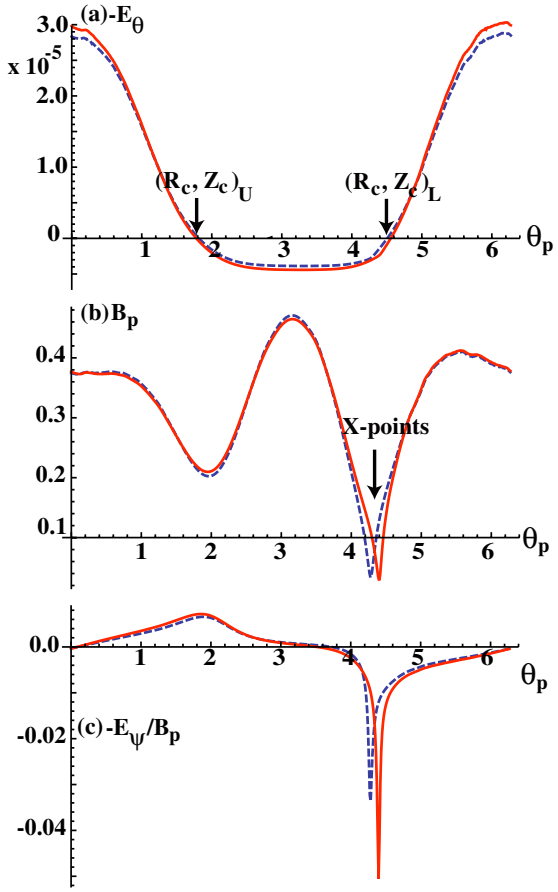

Figure 13. Changes in the fields on a flux surface near the separatrix as lower triangularity δ_L is increased from 0.44 (solid red lines) to 0.54 (dashed blue lines), which decreases the X-point radius R_X (see also figure 9(*a*)). (*a*) The poloidal electric field $-E_\theta$. Note that the lower and upper critical points $(R_c, Z_c)_{L,U}$ where $E_\theta = 0$ do not move appreciably. (*b*) Variation of $B_p = |\nabla\psi|/R$ on the flux surface, showing that the X-point moves closer to the lower critical point at lower δ_L (larger R_X). (*c*) The contribution to $\langle -E_\psi \rangle$ from the region around the X-point increases as it moves closer to the critical point where $-E_\psi$ has its minimum value on the flux surface.

point locations $(R_c, Z_c)_{L,U}$ are essentially unchanged. The X-point, however, moves closer to $(R_c, Z_c)_L$ (figure 13(*b*)) where $-E_\psi$ has a minimum. Recalling that $\langle -E_\psi \rangle = \oint(-\mathrm{d}l_\theta E_\psi/B_p)/\oint(\mathrm{d}l_\theta/B_p)$, where $\mathrm{d}l_\theta$ is the poloidal arc length, in figure 13(*c*) we plot $-E_\psi/B_p$ around the flux surface. Clearly a large portion of the contributions to the integral $\oint(-\mathrm{d}l_\theta E_\psi/B_p)$ comes from poloidal angles near the X-point, and since the X-point is closer to the minimum of $-E_\psi$ for $\delta_L = 0.44$ (the solid red curve), we have

$$\oint_{\delta_L=0.44}\left(\frac{-E_\psi \mathrm{d}l_\theta}{B_p}\right) < \oint_{\delta_L=0.54}\left(\frac{-E_\psi \mathrm{d}l_\theta}{B_p}\right). \tag{26}$$

Thus, $\langle -E_\psi \rangle_{\delta_L=0.44}$ is more negative than $\langle -E_\psi \rangle_{\delta_L=0.54}$, implying a lower P_{LH}. Looking at it from another point of view, since $B_p \sim 0$ near the X-point, the field lines (and plasma) dwell near the X-point much longer than at other points around the flux surface. Since this is a region of more negative radial electric field for the lower δ_L case, the plasma experiences a stronger net negative radial electric field, making the L–H transition easier.

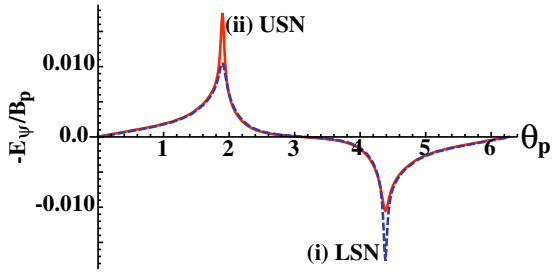

Figure 14. $(-E_\psi/B_\mathrm{p})$ as a function of the poloidal angle θ_p for LSN (dashed blue line) and USN (solid red line) configurations close to a balanced DN, at the points indicated by the labels (i) and (ii) in figures 6(*b*) and 7. Contribution to $\langle -E_\psi \rangle$ for the two cases is essentially identical around the flux surface except near the PF nulls. The dominant contribution comes from the active X-point.

The differences in $\langle -E_\psi \rangle$ between the USN and LSN configurations discussed in section 2.3 (figure 6) can be understood using similar arguments. In figure 14 we plot $(-E_\psi/B_\mathrm{p}) = (\partial\phi/\partial\psi)/B_\mathrm{p}$ as a function of the poloidal angle θ_p for the LSN data point labelled (i) and the USN point labelled (ii) in figures 6(*b*) and 7. The lower X-point is in the vicinity of the critical point $(R_\mathrm{c}, Z_\mathrm{c})_\mathrm{L}$ and makes a negative contribution to the net radial electric field integral. Similarly, the upper X-point is near $(R_\mathrm{c}, Z_\mathrm{c})_\mathrm{U}$ and makes a positive contribution. Which one dominates depends on which one of them is the active X-point where B_p^2 is smaller (closer to zero). Thus the difference between $\langle -E_\psi \rangle_\mathrm{LSN}$ and $\langle -E_\psi \rangle_\mathrm{USN}$ seen in figure 6(*b*) around the symmetric DN data point is entirely due to differing contributions near the two X-points. Of course, in general, other points around the flux surface will make differing contributions for LSN and USN geometries; these two data points ((i) and (ii) in figures 6(*b*) and 7) illustrate the special significance of the X-points.

Variations in $\langle -E_\psi \rangle$ for the other cases discussed in previous sections have similar explanations in terms of geometry-induced changes in the various field components and the related changes in the locations of the X-points with respect to the critical points $(R_\mathrm{c}, Z_\mathrm{c})_\mathrm{L,U}$.

In summary, we believe we have identified an important 'hidden variable' that plays a significant role in determining the L–H transition power threshold P_LH: an intrinsic electric field associated with the Pfirsch–Schlüter currents at the plasma edge. These parallel currents are a robust, collisionality-independent feature of confinement in the toroidal geometry. The electric fields become significant only at the collisional edge close to the separatrix, near the foot of the pedestal that forms in H-mode. Their relevance to the L–H transition derives from the observation that they can either augment or oppose to a varying degree the radial electric field well observed at the transition, depending on the magnetic topology and plasma boundary shape. Thus not only is their source robust (toroidal geometry) but also their influence can be characterized through easily measured, gross features of an equilibrium configuration, without having to require a detailed knowledge of the discharge parameters.

In this work we showed qualitatively but in some detail how these electric fields, in particular the net radial electric field contribution as measured by the flux-surface average $\langle -E_\psi \rangle$, can explain a series of experimental observations:

- In the LSN geometry, the intrinsic radial electric field helps the formation of the negative field well at the edge: $\langle -E_\psi \rangle_\mathrm{LSN} < 0$. For a corresponding USN, $\langle -E_\psi \rangle_\mathrm{USN} = -\langle -E_\psi \rangle_\mathrm{LSN} > 0$, i.e. it opposes the well-formation (figure 6). Experimentally P_LH can differ by more than a factor of 2 for these configurations.
- In LSN, $\langle -E_\psi \rangle$ becomes more negative as the X-point height Z_X is reduced by increasing the lower elongation κ_L (figure 8). Experimentally P_LH is reduced for decreasing Z_X.
- In LSN, $\langle -E_\psi \rangle$ becomes more negative as the X-point radius R_X is increased by reducing the lower triangularity δ_L (figure 9). Experimentally P_LH is reduced for increasing R_X.
- In C-mod USN discharges with the ion ∇B drift pointing down, I-mode can be triggered by *increasing* the upper triangularity δ_U, thus *reducing* R_X. This can be understood in terms of a positive $\langle -E_\psi \rangle$ that becomes less so as δ_U is increased (figure 10). In fact, in this configuration it should be possible to trigger an I–H transition by reducing the X-point radius even further.
- In an L-mode low-power discharge, away from L–H transition threshold, edge radial electric field measurements in DIII-D were found to reverse sign with the reversal of the toroidal field in a LSN discharge. This reversal is reproduced in our calculations (figure 12). In fact, our Pfirsch–Schlüter current-induced field is unique in that this observation cannot be explained by an ion-loss mechanism at the edge.

Thus, we can explain many of the features of the L–H, or the even less well understood L–I transition, that are not captured by a simple scaling law and are generally attributed to 'hidden' variables. Admittedly we are not at the stage yet where we can make quantitative predictions for the power threshold. But we intend to extend this work in directions that should eventually provide more quantitative answers.

Acknowledgments

This research was supported by the Office of Fusion Energy Science of the US Department of Energy under Grant DE-FG02-04ER54742.

References

[1] ITER Physics Expert Group on Confinement and Transport 1999 *Nucl. Fusion* **39** 2175
[2] Wagner F., Becker G., Behringer K. and ASDEX Team 1982 *Phys. Rev. Lett.* **49** 1408
[3] Shaing K.C. and Crume E.C. 1989 *Phys. Rev. Lett.* **63** 2369
[4] Hahm T.S. and Burrell K.H. 1995 *Phys. Plasmas* **2** 1648
[5] Burrell K.H. 1997 *Phys. Plasmas* **4** 1499
[6] Connor J.W. and Wilson H.R. 2000 *Plasma Phys. Control. Fusion* **42** 1
[7] Gohil P. 2002 *Plasma Phys. Control. Fusion* **44** 37
[8] Osborne T.H. 1990 *Nucl. Fusion* **30** 2023
[9] Ryter F. and the International H-Mode power threshold database activity 2002 *Plasma Phys. Control. Fusion* **44** A415

[10] Maingi R. *et al* 2010 Overview of L–H power threshold studies in NSTX *Nucl. Fusion* **50** 064010
[11] Fukuda T. 1998 'Hidden' variables affecting the L–H transition *Plasma Phys. Control. Fusion* **40** 543
[12] Ryter F. and the H-Mode Database Working Group 1996 *Nucl. Fusion* **36** 1217
[13] Andrew Y., Hawkes N.C., O'Mullane M.G. and JET EFDA Contributors 2004 *Plasma Phys. Control. Fusion* **46** A87
[14] Kalupin D., Andrew Y., Corrigan G., Parail V. and JET EFDA Contributors 2010 *Contrib. Plasma Phys.* **50** 356
[15] Carlstrom T.N. 2005 L–H transition and power threshold studies in the DIII-D tokamak *Fusion Sci. Technol.* **48** 997
[16] Gohil P., Evans T.E., Fenstermacher M.E., Ferron J.R., Osborne T.H., Park J.M., Schmitz O., Scoville J.T. and Unterberg E.A. 2011 *Nucl. Fusion* **51** 103020
[17] Meyer H. *et al* ASDEX Upgrade the MAST and NSTX Teams 2006 *Nucl. Fusion* **46** 64
[18] LaBombard B. *et al* and the Alcator C-Mod Team 2005 *Phys. Plasmas* **12** 056111
[19] Carlstrom T.N., Gohil P., Watkins J.G., Burrell K.H., Coda S., Doyle E.J., Groebner R.J., Kim J., Moyer R.A. and Rettig C.L. 1994 Experimental survey of the L–H transition conditions in the DIII-D tokamak *Plasma Phys. Control. Fusion* **36** 147
[20] Carlstrom T.N., Groebner R.J. and Rhodes T.L. 2001 Dependence of the H-mode power threshold on plasma shape in DIII-D *43rd Annual Meeting of the APS Division of Plasma Physics (Long Beach, CA, 29 October–2 November 2001)* Abstract LP1.010 http://flux.aps.org/meetings/YR01/DPP01/abs/S1600010.html
[21] Zakharov L.E., Gorelenkov N.N., White R.B., Krasheninnikov S.I. and Pereverzev G.V. 2004 Ignited spherical tokamaks and plasma regimes with Liwalls *Fusing Eng. Des.* **72** 149
[22] Mazzucato E. 2011 *AIP Adv.* **1** 012101
[23] Hazeltine R.D. and Meiss J.D. 1992 *Plasma Confinement* (Reading, MA: Addison-Wesley)
[24] Boozer A.H. 1986 *J. Plasma Phys.* **35** 133
[25] Chang C.S., Seunghoe K. and Weitzner H. 2002 *Phys. Plasmas* **9** 3884
[26] Kadomtsev B.B. and Pogutse O.P. 1965 *Rev. Plasma Phys.* vol 5 (New York: Consultants Bureau) p 261
[27] Hazeltine R.D. and Hinton F.L. 1973 *Phys. Fluids* **16** 1883
[28] Aydemir A.Y. 2009 An intrinsic source radial electric field and edge flows in tokamaks *Nucl. Fusion* **49** 065001
[29] Aydemir A.Y. 2007 Shear flows at the tokamak edge and their role in core rotation and the L–H transition *Phys. Rev. Lett.* **98** 225002
[30] Ivanov A.A., Khayrutdinov R.R., Medvedev S.Yu. and Poskekhonov Yu.Yu. 2006 The spider code—axisymmetric fixed boundary plasma equilibrium solver, preprint no 7, keldysh institute of applied mathematics http://www.keldysh.ru/papers/2006/prep07/prep2006_07.html
[31] Jackson J.D. 1990 *Classical Electrodynamics* (New York: Wiley)
[32] Fenzi C., McKee G.R., Fock R.J., Burrell K.H., Carlstrom T.N., and Groebner R.J. 2005 Effect of ion ∇B drift direction on density fluctuation poloidal flow and flow shear *Phys. Plasmas* **12** 062307
[33] Xu X.Q., Dudson B., Snyder P.B., Umansky M.V. and Wilson H. 2010 Nonlinear simulations of peeling–ballooning modes with anomalous electron viscosity and their role in edge localized mode crashes *Phys. Rev. Lett.* **105** 175005
[34] Carlstrom T.N. *et al* 2000 Edge E_r structure and the ∇B drift effect on L–H transition *27th EPS Conf. on Controlled Fusion and Plasma Physics (Budapest, 12–16 June 2000)* ECA 24B p 756 http://epsppd.epfl.ch/Buda/web/contents.htm
[35] Carlstrom T.N., Groebner R.J., Fenzi C., McKee G.R., Moyer R.A. and Rhodes T.L. 2002 Evidence for the role of velocity shear on the L–H transition in DIII-D *Plasma Phys. Control. Fusion* **44** 333
[36] Maingi R. *et al* 2005 H-mode pedestal, ELM and power threshold studies in NSTX *Nucl. Fusion* **45** 1066
[37] Connor J.W. and Pogutse O.P. 2001 *Plasma Phys. Control. Fusion* **43** 281
[38] Wilson H.R., Snyder P.B., Huysmans G.T.A. and Miller R.L. 2002 *Phys. Plasmas* **9** 1277
[39] Kurita G., Nagashima K., Kikuchi M., Ushigusa K., Neyatani Y., Ozeki T., Tokuda S. and Azumi M. 1999 *Plasma Phys. Control. Fusion* **41** 159
[40] Snyder P.B., Wilson H.R., Ferron J.R., Lao L.L., Leonard A.W., Osborne T.H., Turnbull A.D., Mossessian D. and Xu X.Q. 2002 *Phys. Plasmas* **9** 2037
[41] Chang C.S., Kue S. and Weitzner H. 2004 *Phys. Plasmas* **11** 2649
[42] Whyte D.G. *et al* and the Alcator C-Mod Team 2010 I-mode: an H-mode energy confinement regime with L-mode particle transport in Alcator C-MOD *Nucl. Fusion* **50** 105005